JGR Space Physics

Ionospheric Boundaries Derived From Auroral Images

G. Chisham[1] , **A. G. Burrell[2]** , **E. G. Thomas[3]** , and **Y.-J. Chen[4]**

[1]British Antarctic Survey, Cambridge, UK, [2]Space Science Division, US Naval Research Laboratory, Washington, DC, USA, [3]Thayer School of Engineering, Dartmouth College, Hanover, NH, USA, [4]University of Texas at Dallas, Richardson, TX, USA

Abstract This paper presents updated methods for locating the Poleward and Equatorward Auroral Luminosity Boundaries (PALB and EALB) directly from IMAGE Far UltraViolet (FUV) images of the Northern Hemisphere auroral oval. Separate boundaries are determined from images measured at different FUV wavelengths. In addition, new methods for indirectly estimating the Open-Closed magnetic field line Boundary (OCB) and the Equatorward Precipitation Boundary (EPB) locations are presented; these new boundaries are derived from a combination of the auroral luminosity boundary estimates with statistical latitudinal offsets derived from comparisons with low-altitude spacecraft Particle Precipitation Boundaries (PPBs). Subsequently, we derive new circle model fits for all these boundary data sets, as well as new quality control criteria for these model fits. The suitability of circle fits for each of the data sets is discussed, and the OCB and PALB circle fits are validated against the Convection Reversal Boundary (CRB), as measured by low-altitude in situ spacecraft. All the new boundary data sets, covering the epoch May 2000 to October 2002, are freely available online.

Plain Language Summary The ability to measure and model near-Earth space, its response to driving forces in the interplanetary solar wind, and the impact of these forces on the Earth's upper atmosphere is the basis for the understanding and forecasting of space weather. Because there is a strong physical connection between the Earth's magnetosphere (the region of near-Earth space dominated by the Earth's magnetic field) and ionosphere (the ionized region of the upper atmosphere) near the poles, observations of the ionosphere provide information about the magnetospheric state. Dynamic processes within the magnetosphere accelerate electrons and ions within the space environment giving them the energy to precipitate in the upper atmosphere. These high-energy charged particles excite atmospheric atoms and molecules, creating aurora. The light from the aurora can be observed at ultraviolet wavelengths by space-based imagers. In this study we identify the higher and lower latitude edges of the aurora and determine their relationship to important particle boundaries. Circles are then fitted to the spatial boundary variations to make sure they are defined across all longitudes. These data sets can be used to identify and track the spatial extent and dynamics of magnetospheric regions and boundaries.

1. Introduction

The Earth's magnetosphere covers a vast region of near-Earth space, but in situ measurements of magnetospheric dynamics are limited to a small number of Earth-orbiting spacecraft that can only provide single-point measurements at a particular time. Extending these measurements to describe the whole system relies on interpolation, extrapolation, speculation, or the use of magnetospheric models. However, at high latitudes the terrestrial ionosphere couples with the outer regions of the magnetosphere with progressively higher latitudes coupling to regions further from the Earth (S. W. H. Cowley, 2000; Kivelson et al., 1996). This Magnetosphere-Ionosphere (MI) coupling means that ionospheric dynamics and properties can provide insights about the state of the magnetosphere.

Magnetospheric regions can be categorized in different ways, such as defining regions by the local particle populations or currents. One of the simplest divisions is the separation of the magnetosphere into regions defined by their different magnetic field topologies (Dungey, 1961; Milan et al., 2017):

1. "Open" magnetic field lines connect directly from the geomagnetic field to the Interplanetary Magnetic Field (IMF) that emanates from the Sun, and expands throughout the solar system. These field lines converge into the geomagnetic polar regions, forming the polar caps.

2. "Closed" magnetic field lines are geomagnetic field lines that exist wholly within the geospace domain, connecting directly from the Southern to the Northern Hemisphere ionosphere, equatorward of the polar caps, with no direct connection to the IMF.

The boundary between these topologically-different magnetospheric regions is commonly known as the Open-Closed magnetic field line Boundary (OCB) (Lockwood, 1998).

One way of identifying different magnetospheric regions and boundaries is through auroral precipitation into the ionosphere (Kilcommons et al., 2017; Newell et al., 2004). The auroral region is immediately equatorward of the ionospheric signature of the OCB and is characterized by a range of different auroral forms that provide information about associated magnetospheric dynamics. At the poleward edge of the auroral region, auroral emissions change as a result of the transition from closed to open field lines at the OCB. At the equatorward edge of the auroral region the disappearance of auroral emissions results from the reduction in precipitating particles to low levels, although precipitation can often be measured equatorward of the auroral emission boundary. The Equatorward Precipitation Boundary (EPB) can be measured by low altitude spacecraft and matches well with the low latitude boundary of solar wind-driven ionospheric plasma convection (Greenwald et al., 2002).

The magnetospheric system is highly dynamic, as it (and consequently, the coupled ionosphere) responds to changes in driving forces in the solar wind, as well as to atmospheric losses (such as Joule heating) and losses to the interplanetary medium (such as substorm plasmoid ejections) (Chisham et al., 2008; Milan et al., 2003). Both the polar cap and the auroral regions expand and contract in response to magnetic reconnection driven by both solar wind and internal magnetospheric dynamics. Consequently, the OCB, the EPB, and the auroral region between them are in continual motion (S. Cowley & Lockwood, 1992; Milan et al., 2003, 2012; Siscoe & Huang, 1985). Hence, many aspects of MI science, as well as space weather applications, require the regular measurement or estimation of the locations of these boundaries (Newell et al., 2014; Zhu et al., 2020).

It is possible to identify different regions and boundaries in the ionosphere as the characteristics of the precipitation of particles from the magnetosphere into these different ionospheric regions (polar cap, auroral region, sub-auroral region) are distinct. This is due to differences in the plasma in the magnetospheric regions they map to (Sotirelis & Newell, 2000). These changes in precipitation are best measured by plasma detectors on spacecraft in low-Earth orbit, which provide highly accurate and precise boundary identifications at single locations (e.g., Newell et al., 1991, 1996). The drawback of such observations is that they provide infrequent and sparse estimates of a boundary, which makes them unsuitable for providing comprehensive spatio-temporal pictures of the boundaries and their motion. Such comprehensive boundary definitions are required both to improve the high-latitude specifications for space weather modeling, and to facilitate statistical studies of the polar region (Burrell, Chisham, Milan, et al., 2020; Chisham, 2017a; Kilcommons et al., 2017; Newell et al., 2004, 2014; Redmon et al., 2010).

Fortunately, there are other ground- and space-based instruments that can observe larger regions of the high-latitude ionosphere, allowing a more complete mapping of the regions and boundaries. From the ground, both coherent and incoherent scatter radars (Aikio et al., 2006; Blanchard et al., 2001; Chisham et al., 2007; Chisham & Freeman, 2003), as well as photometers and all-sky cameras (Blanchard et al., 1995; X.-C. Chen et al., 2017) have been used to locate boundaries in the ionosphere. On a larger scale, the Active Magnetosphere and Planetary Electrodynamics Response Experiment (AMPERE) (Anderson et al., 2014; Coxon et al., 2018) and the SuperMAG archive of global ground-based magnetometer data (Gjerloev, 2012) provide full-hemispheric coverage of high-latitude magnetic field variability, providing maps of MI current systems. Space-based auroral images, through their extensive coverage of the auroral oval, are probably the best tool for identifying the spatial extent of the auroral region, and provide the ability to monitor both the OCB and EPB simultaneously. There is a long history of determining the poleward edge of the auroral oval from space-based auroral imager data (Baker et al., 2000; Boakes et al., 2008; Carbary et al., 2003; Kauristie et al., 1999; Longden et al., 2010). This boundary has regularly been used as a proxy for the OCB in order to study processes occurring there, like magnetic reconnection (Chisham et al., 2008; Hubert et al., 2006, 2010).

In this paper, we present boundaries derived from the Far UltraViolet (FUV) imagers on the Imager for Magnetopause-to-Aurora Global Exploration (IMAGE) spacecraft (Mende, Heetderks, Frey, Lampton, Geller, Habraken, et al., 2000). The Northern Hemisphere IMAGE epoch has proved an extremely good data set for

studies of space weather (Boakes et al., 2009, 2011; Frey et al., 2004; Milan, 2009; Milan et al., 2009; Mooney et al., 2020, 2021). Longden et al. (2010) presented a reliable, automated method to estimate the location of Poleward Auroral Luminosity Boundaries (PALBs) and Equatorward Auroral Luminosity Boundaries (EALBs) in IMAGE FUV measurements. Here, we introduce additional selection criteria that remove potentially unreliable boundaries from the Longden et al. (2010) data sets. We also present new methods for estimating the OCB and EPB from the measured PALBs and EALBs, respectively. We also model all these boundary data sets with circles using the method outlined by Chisham (2017a), with the important addition of a figure of merit that allows the reliability of the data to be more easily assessed. These fitted circle versions of the boundaries allow easier implementation into models and certain data analysis applications. Finally, the new OCB circle data set is validated in a method similar to the IMAGE OCB validation performed in Burrell, Chisham, Milan, et al. (2020).

2. Instrumentation

2.1. IMAGE FUV

The IMAGE spacecraft (Burch, 2000; Gibson et al., 2000) was launched on 25 March 2000. One of the key aims of the mission was to simultaneously image both proton and electron aurora using three FUV imagers. The data set described in this paper was compiled from IMAGE FUV images of the Northern Hemisphere auroral regions extending from May 2000 to October 2002, during which time the spacecraft was located within a highly elliptical polar orbit with an inclination of 90°. The orbit apogee during this time was positioned over the Northern Hemisphere polar ionosphere at ~7 R_E; the orbit perigee was located in the upper regions of the Southern Hemisphere ionosphere, at ~1,000 km altitude. The orbital period was ~13.5 hr, allowing imaging of the Northern Hemisphere auroral oval for most of this time.

The FUV instrument on the IMAGE spacecraft (Mende, Heetderks, Frey, Lampton, Geller, Habraken, et al., 2000) comprised three imagers: The Spectrographic Imagers (SI), termed SI12 and SI13 (Mende, Heetderks, Frey, Stock, et al., 2000), and the Wideband Imaging Camera (WIC) (Mende, Heetderks, Frey, Lampton, Geller, Abiad, et al., 2000). All three imagers had a temporal resolution of ~2 min. The SI12 imager measured Doppler-shifted Lyman-α emissions at 121.8 nm that occur as a result of proton precipitation. The SI13 imager measured oxygen emissions at 135.6 nm that occur as a result of energetic electron precipitation. The WIC imager measured emissions in the N_2 Lyman-Birge-Hopfield band (140–190 nm) that occur as a result of electron precipitation. Images from both the SI imagers had a resolution of 128 × 128 pixels, whereas those from the WIC imager had a resolution of 256 × 256 pixels.

The high spatial resolution of the imagers and the near-perpendicular pointing angles around apogee resulted in good images of the complete auroral oval for much of the orbit. However, as the spacecraft approached perigee the images were taken from increasingly oblique angles. As a consequence of this, the entirety of the auroral oval was not captured in these images and the auroral features are increasingly smeared. Thus, boundary determinations from the images taken at these points in the orbits are less accurate. Additional uncertainties in boundary determinations also result from minor inaccuracies in the spacecraft pointing direction and from the challenges of dealing with dayglow. The impacts of these issues on the boundary locations are discussed in full detail by Longden et al. (2010).

2.2. DMSP

The Defense Meteorological Satellite Program (DMSP) consists of a constellation of polar orbiting, sun-synchronous satellites in low Earth orbit (~830 km altitude). Data from the Special Sensor J (SSJ)/4 instruments (Hardy et al., 1984) on each spacecraft allowed the accurate identification of the locations of ionospheric Particle Precipitation Boundaries (PPBs) along the DMSP orbits. These PPBs occur where the boundaries between magnetospheric regions characterized by different ion and electron distributions map to the ionosphere. The orbital period of the DMSP spacecraft was ~101 min, and ion and electron energy spectra were measured every second, which corresponds to a potential spatial resolution of the boundary determinations along the orbit of ~7.5 km (~0.1° latitude).

The algorithms used to identify PPBs in the DMSP data are different for measurements made in the dayside and nightside portions of the ionosphere, due to the local time differences in the particle precipitation regions.

The algorithm used for automated identification of dayside PPBs from the DMSP energy spectra is detailed in Sotirelis and Newell (2000), and is based on boundaries between the dayside precipitation regions classified by Newell et al. (1991). The "doc" boundary, which represents an unambiguous transition between open and closed precipitation regions, is taken as the best estimate of the OCB on the dayside. The "deq" boundary, which is located at the equatorward edge of diffuse precipitation, is taken as the EPB on the dayside.

The algorithm used for automated identification of nightside PPBs from the DMSP energy spectra is detailed in Newell et al. (1996) and Sotirelis and Newell (2000). The "b6" boundary on the nightside, which represents the poleward edge of the subvisual auroral drizzle that occurs poleward of the main auroral oval, is taken as the best proxy for the OCB on the nightside. The most equatorward of the "b1e" boundary (the "zero-energy" electron convection boundary) and the "b2i" boundary (the ion isotropy boundary) is taken as the EPB on the nightside.

Following Sotirelis and Newell (2000), if multiple crossings of the same magnetospheric precipitation region are identified on a single spacecraft overpass, then the most poleward boundary for each region is used in the determination of the OCB and the most equatorward boundary for each region is used in the determination of the EPB. Where clear transitions between precipitation regions cannot be made, the PPBs are not used in this analysis. These post-processing checks identify failures of the boundary algorithm, and remove ambiguous boundaries.

Data from the Ion Velocity Meter (IVM) on the DMSP spacecraft (Heelis & Hanson, 1998) are also used to identify Convection Reversal Boundaries (CRBs) that are used here for validation of the poleward boundaries (Burrell, Chisham, Milan, et al., 2020; Y.-J. Chen et al., 2015). These CRBs indicate where the ionospheric plasma drifts change from moving sunward to anti-sunward (or vice versa). The locations of the CRBs have lower uncertainties when the plasma density is high and a high-fidelity signal is returned. Hence, the CRB data set is biased to local summer months (May–August) in the Northern Hemisphere.

During the epoch of the IMAGE FUV observations, PPBs were available from four DMSP spacecraft: F12, F13, F14, and F15. CRBs were available from F13 and F15. The Northern Hemisphere orbit of DMSP F13 was approximately dawn to dusk in AACGM co-ordinates, whereas the DMSP F12, F14, and F15 orbits were approximately in the pre-noon to post-dusk direction. These restrictions in the available orbits mean that there are no DMSP measurements in the pre-midnight and early morning sectors in the Northern Hemisphere.

3. Pre-Existing IMAGE FUV Boundary Determination Methods and Data Sets

The new auroral luminosity boundary data sets presented here are refinements of those determined by Longden et al. (2010). The method of Longden et al. (2010) was based on that of Boakes et al. (2008), who first developed an automated method for identifying boundaries in the IMAGE FUV data. Longden et al. (2010) improved this methodology in several ways, the most important of which was adding the ability to deal with the presence of bifurcated auroral ovals (which they showed can comprise up to 50% of the data base in the midnight sector during active geomagnetic times). This method requires no prior knowledge of the presence of bifurcations in the oval; it involves the fitting of two different functions to the data to deal with the possibility of both single and double ovals. The Longden et al. (2010) methodology also allows the estimation of the PALBs and EALBs with no prior knowledge of the level of auroral activity (i.e., the method is not based on fixed intensity thresholds as some previous boundary determination methods were).

Here, we present a brief overview of the Longden et al. (2010) methodology:

1. The data in each auroral image are divided into 24 regional segments in the Altitude-Adjusted Corrected GeoMagnetic (AACGM) latitude and Magnetic Local Time (MLT) coordinate system (Shepherd, 2014), each segment covering 1 hr of MLT.
2. For each 1 hr MLT segment, a latitudinal intensity profile is constructed by finding the average pixel intensity in bins of 1° AACGM latitude in the range 50°–90°.
3. Two separate model functions are fitted to each latitudinal intensity profile:
    (a) a function with a single Gaussian component and a quadratic background, and
    (b) a function with two Gaussian components and a quadratic background.
4. Of the two fitted functions, the better model for that profile is chosen by determining the reduced χ^2 goodness-of-fit statistic for both functions. This is performed separately for the latitudinal intensity profiles measured at each MLT.

5. When the single Gaussian function provides the better fit, the location of the PALB is estimated as being offset poleward from the location of the center of the Gaussian peak by the Full Width at Half Maximum (FWHM) of the Gaussian profile, whereas the EALB is estimated as being offset equatorward from the center of the Gaussian peak by the FWHM. When the double Gaussian function provides the better fit, the location of the PALB is estimated as being offset poleward from the location of the poleward peak of the two Gaussian components by the FWHM of that peak, whereas the EALB is estimated as being offset equatorward from the location of the equatorward peak of the two Gaussian components by the FWHM of that peak.

6. Criteria are applied both during and after the fitting process to discard boundaries where the fitting has been poor, or the data incomplete. However, as with any automated technique it has its limitations, and high-latitude sun-aligned arcs, and subauroral features such as detached arcs and patches may occasionally result in inaccurate modeling of the boundaries (see Longden et al. (2010) for full details).

The analyses of Boakes et al. (2008) and Longden et al. (2010) showed that the PALBs determined from the three different FUV imagers are not co-located with each other; neither are they co-located with the PPB estimates of the OCB, which are generally accepted as the most accurate markers of the OCB. The offsets between the different measurements are a result of the separate behavior of ions and electrons on magnetic field lines close to the boundary. In order to estimate the most probable OCB locations from the measured PALB locations, Longden et al. (2010) determined statistical latitudinal offsets between the measured PALBs and DMSP estimates of the OCB. They also determined the variation of these statistical offsets with MLT. These offsets for the original PALBs from each FUV imager were published by Longden et al. (2010). The original Longden PALB and EALB data sets are freely available (Chisham, 2017b).

Subsequent studies have shown the usefulness of this original data set. Longden et al. (2014) used these data to study the local time variation and scaling of poleward auroral boundary dynamics. Mooney et al. (2020) used the data set to study the spatio-temporal variation of the OCB through the substorm cycle. They followed up this work by using the IMAGE boundary data to evaluate auroral forecasts (Mooney et al., 2021). Recently, Hoque et al. (2021) have used the data set to evaluate convection reversal boundaries measured by the SuperDARN radars.

Following the work of Longden et al. (2010), Chisham (2017a) showed that by assuming that the PALBs are well modeled by circles (in AACGM co-ordinates), then these data sets can be more practically used in the development of new ionospheric climatologies and empirical models. In this new methodology, empirical data are binned in a co-ordinate system that adapts relative to the position of the boundary. Chisham (2017a) presented a demonstration of how this methodology can be used to improve the climatological representation of ionospheric vorticity. The derived PALB circle fits form a key part of the OCBpy python data analysis package (Burrell, Chisham, & Reistad, 2020).

4. New Boundary Determination Methods and Data Sets

4.1. Changes to Existing Boundary Acceptance Criteria

The new PALB and EALB data bases are a subset of the Longden et al. (2010) data sets. In the creation of the new PALB and EALB data bases, changes have been made to the previously published methodology to deal with two separate issues.

4.1.1. Edge of Field of View Issues

The original boundary-determination algorithm developed by Longden et al. (2010) didn't adequately consider problems that might be introduced owing to the location of the edge of the instrument field of view. In Longden et al. (2010), acceptance criterion 2 in Section 3.2 of that paper stated - "The Gaussian center(s) μ must fall within the AACGM latitude range of the given intensity profile." This criterion required that more than half of the latitudinal auroral intensity variation had been observed, but did not require that the estimated boundary location itself was within the field of view. This criterion occasionally introduced issues when there were anomalous or missing intensity values at the edge of the field of view which resulted in the appearance of a false peak in the latitudinal intensity profile. It also introduced biases if the observable portion of the auroral profile at the edge of the field of view was not strictly Gaussian. As a consequence of these issues, the Longden algorithm often placed boundaries equatorward of the image field of view without having observed the whole profile.
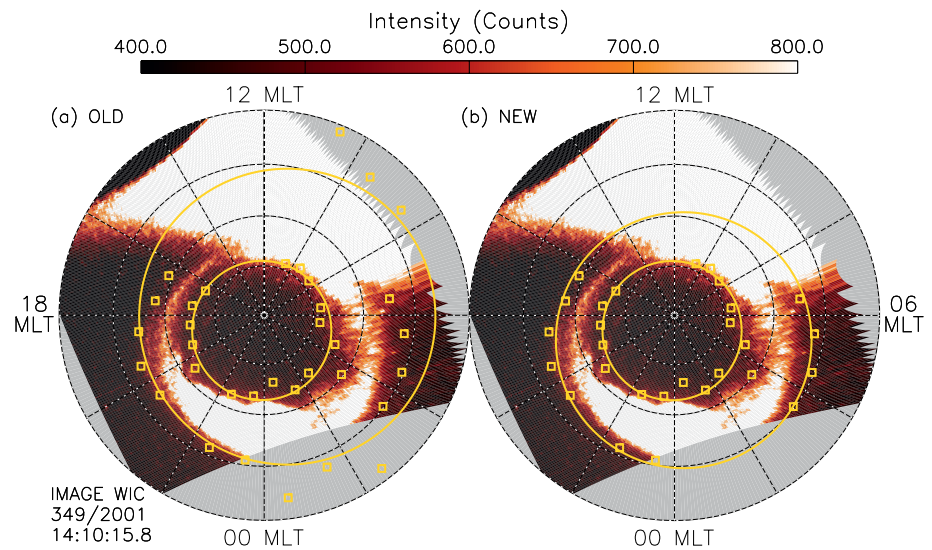
Figure 1. Auroral images measured by the WIC FUV imager at 14:10 UT on 15 December 2001 (day 349). Poleward Auroral Luminosity Boundaries (PALBs) and Equatorward Auroral Luminosity Boundaries (EALBs) are shown on the figure as yellow squares using (a) the original Longden boundary data set, and (b) applying the new data selection criteria. The yellow solid lines show circle fits to the PALBs and EALBs.

Figure 1a presents an example WIC image where some of the boundaries (yellow squares) have been evaluated to be equatorward of the image field of view. On the dayside, where dayglow dominates the image, variations in the dayglow intensity have resulted in false EALBs equatorward of the field of view. In the main auroral oval on the nightside, EALBs have also been placed equatorward of the edge of the field of view. Although there are often instances where this boundary placement may be accurate, in this instance partially observed latitudinal intensity profiles that are not strictly Gaussian have led to the EALBs being placed further equatorward than they are likely to be. Not requiring the observation of the full auroral profile within the field of view has led to these erroneous boundary placements. The solid yellow circles show circle fits to the PALB and EALB locations (see Section 5). The EALB circle fit is heavily affected by the erroneous EALB estimates.

We have amended the original criterion such that boundaries in the new data set instead need to be in a 1° AACGM latitude bin that contains good data and lies at least 2 pixels inward from the edge of the IMAGE field of view. This minimizes the impact of these edge effects in most cases. Figure 1b presents the boundaries from the revised data set for the same time interval; the EALBs that were originally placed outside of the field of view have been removed from the image. Consequently, the EALB fitted circle is now more representative of the true equatorward edge of the auroral oval. As shown in this example, this problem is more of an issue for the EALBs than the PALBs as the EALBs are typically closer to the edge of the image field of view. This issue is most pertinent for images taken when the IMAGE spacecraft was close to perigee; at these times the spatial area of the ionosphere contained within the field of view of each image was reduced and the auroral oval often extended outside of the image field of view.

4.1.2. Anomalous Mapping Issues

Within the Longden et al. (2010) IMAGE FUV data base there are occasional orbits for which the image mapping to the ionosphere for particular imagers is in error. These anomalies in the Longden data base were identified through the comparison of the parameters of circle fits to the PALBs and EALBs (see Section 5) for the three FUV imagers along a complete polar orbit. This anomalous mapping is also clear in individual comparisons of simultaneous images from all three FUV imagers.

Figure 2 presents an example that shows this anomalous mapping; it presents images from 06:51:53 UT on 30 September 2000 (day 274) as measured by (a) SI12, (b) SI13, and (c) WIC. Although the auroral ovals viewed by SI12 and WIC show slightly different features (as expected for proton and electron aurora), the PALBs and EALBs determined from the auroral profiles are very similar, and the oval is centred close to the AACGM pole. However, the auroral oval in the SI13 image, whilst showing similar features to the WIC aurora (they both
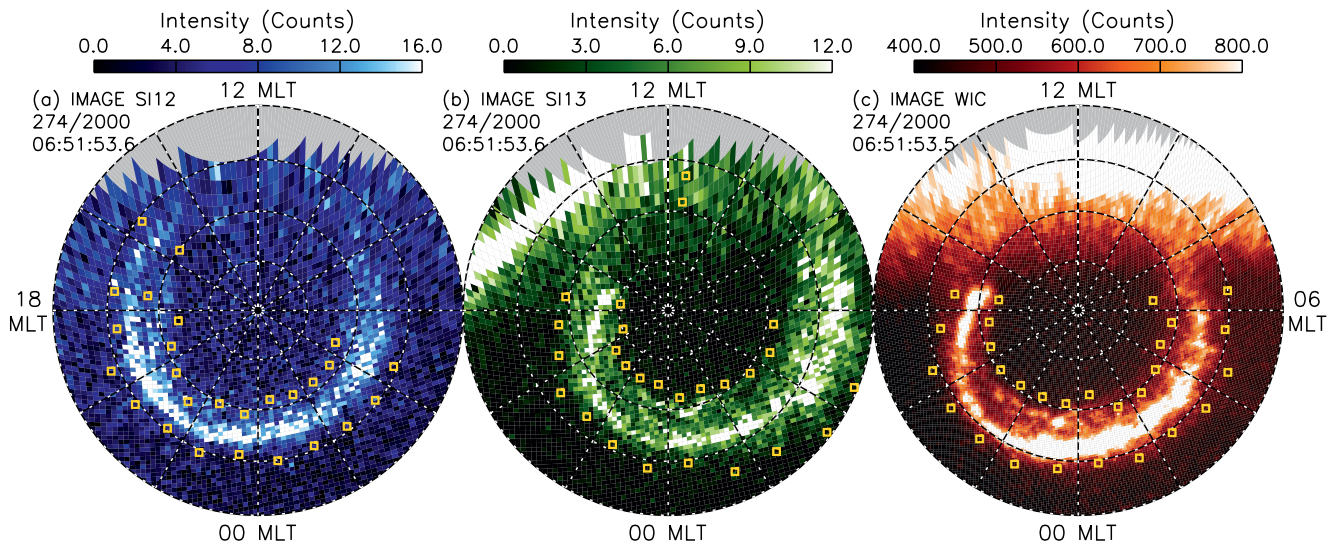
Figure 2. Auroral images measured by the IMAGE FUV imagers at 06:52 UT on 30 September 2000 (day 274), from (a) the SI12 imager, (b) the SI13 imager, and (c) the WIC imager. The yellow squares indicate the locations of the Poleward Auroral Luminosity Boundaries (PALBs) and Equatorward Auroral Luminosity Boundaries (EALBs) determined using the original Longden methodology.

represent electron aurora), is shifted significantly toward dawn (by ∼5°–7°). This anomalous shift in the mapped SI13 auroral position persists throughout this orbit.

Boundaries determined from data in the orbits in the Longden data base that are affected by this anomalous mapping have been removed from the new PALB and EALB data sets. This issue resulted in the removal of ∼2% of the data base, predominantly SI12 and SI13 data. It is possible that future analysis may provide the opportunity to correct this mapping problem and for these intervals to be included in future versions of the IMAGE FUV boundary data.

4.2. PALB

A summary of the new PALB data base is presented in Figure 3. The black solid line shows the variation with MLT of the median PALB latitude for each imager: (a) SI12, (b) SI13, and (c) WIC. The thick error bars at each MLT show the latitude range from the lower to the upper quartile of the measured PALB latitudes, whereas the thinner bars show the latitude range from the 10%–90% percentiles. Although the variations for the three imagers are similar, there are subtle differences in the median latitudes of the different boundaries (as discussed above),
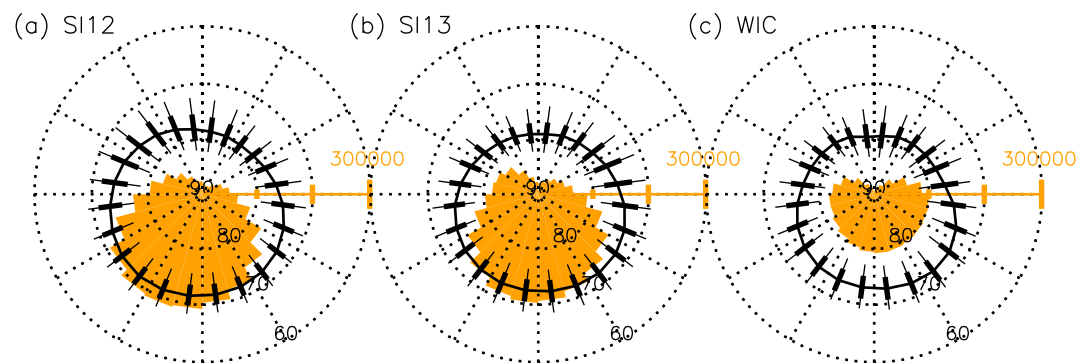

Figure 3. Statistics of Poleward Auroral Luminosity Boundaries (PALB) locations identified in data from the IMAGE FUV imagers (a) SI12, (b) SI13, and (c) Wideband Imaging Camera (WIC), in AACGM and Magnetic Local Time (MLT) co-ordinates. The solid black line describes the MLT variation of the median PALB latitude. The thick black error bars present the quartile latitude variation at each MLT. The thin black error bars at each MLT present the extent of the distribution from the 10%–90% percentile. The orange histograms present the number of PALB observations in each MLT sector.

particularly in the SI12 variation, which extends to lower latitudes in the afternoon sector. This is probably owing to differences in the relationship of electron and proton precipitation to the OCB in this sector.

The orange histograms in each map highlight the number of boundaries measured in each MLT sector across the whole measurement epoch. This shows that for all the imagers a larger number of boundaries are measured in MLT sectors in the nightside ionosphere ($\sim10^5$), where the auroral emissions are strongest and where there is less contamination of the images by dayglow. The number of boundaries decreases significantly toward noon, where the number of observed boundaries is lower ($\sim10^4$). The variation shown in Figure 3 is similar to that of the original PALB data set as was presented in Figure 4a of Longden et al. (2010). The main difference here is the reduction in the number of WIC boundaries from dawn, through noon, to dusk. This is because the new criterion now excludes potentially erroneous boundaries in the original data set that were complicated by the effects of dayglow. Whereas the number of WIC boundaries in the original data set peaked around dawn and dusk, now the peak is near midnight, consistent with the other two imagers.

These data bases are located in the files PALB_SI12_v2, PALB_SI13_v2, and PALB_WIC_v2 in the directory "raw_boundaries" at https://doi.org/10.5285/fa592594-93e0-4ee1-8268-b031ce21c3ca (Chisham, 2022).

4.3. OCB

In the original studies of Boakes et al. (2008) and Longden et al. (2010) the PALBs were compared with DMSP OCB proxies to determine statistical latitudinal offsets between the boundaries. In these studies, the latitudinal offsets were determined separately for each imager in each MLT sector (see the methods presented in those papers). However, with three imagers this methodology leads to three distinct estimates of the OCB rather than one. This can lead to difficulties when explaining the differences between disparate OCB estimates from different data sets (e.g., Mooney et al., 2020).

Here, we present a new methodology that combines boundary data from all the imagers and their relationships with the DMSP OCB proxy to make a single best estimate of the OCB location at each time. The statistical comparisons between the IMAGE PALBs and the DMSP OCB estimates are here treated differently to the methods used by Boakes et al. (2008) and Longden et al. (2010). First, we are more selective about which DMSP data are used in the comparison. This is important because the quality of the DMSP precipitation boundaries can be affected by a variety of different sources of uncertainty, including the presence of nuisance signals and magnetic perturbations (Kilcommons et al., 2017). Figure 4 displays as orange dots the locations of all the OCB estimates from the four different DMSP spacecraft used over the epoch of the study (DMSP F12, F13, F14, and F15). For each spacecraft the boundaries appear in fixed bands dictated by their orbits. The DMSP orbits cross the polar regions at fixed local times in geographic co-ordinates, but these spread into bands when the orbits are transformed into the AACGM and MLT co-ordinate system. The black error bars and solid line in Figure 4 represent the variation of the median and quartile SI13 PALBs with MLT for reference, as presented in Figure 3.

In Figure 4 we have split the observed DMSP OCBs into two groups; those measured at MLTs and latitudes within the enclosed red regions and those measured at MLTs and latitudes outside of these regions. We define the areas within the red regions as those where the DMSP OCB estimates are most reliable for use in our statistical comparisons. There are two reasons why we only use the observed OCBs from within the red regions:

1. In the MLT sectors within the red regions, the DMSP orbits cover the full AACGM latitude range where the OCB is likely to be. Outside of the red regions, due to the restricted spacecraft orbits, the latitudinal distibution of the observed OCBs is truncated on the equatorward side. Comparing the OCBs with the PALBs in these MLT sectors leads to a bias in the statistical offsets owing to a biased distribution of uncertainties in the OCB observations. This unreliability in the statistical offset is greatest in the MLT sectors where the latitudinal distribution is most truncated.
2. Boundaries are sharper and more easily identified in the DMSP data when the spacecraft orbit is such that it crosses the boundary close to the perpendicular direction. Comparing the spread of the orbits with the SI13 median PALB variation in Figure 4 shows that for those orbits that pass closer to the AACGM pole, the DMSP orbit passes closer to perpendicular to the median PALB location. These DMSP OCB estimates will tend to be the most accurate. For the OCBs determined in MLT sectors outside of the red regions, the DMSP orbits are close to being parallel with the median PALB location. In some cases these orbits will be "skimming" the boundary, and for many of the boundaries determined in this region, the boundary transition will be spread
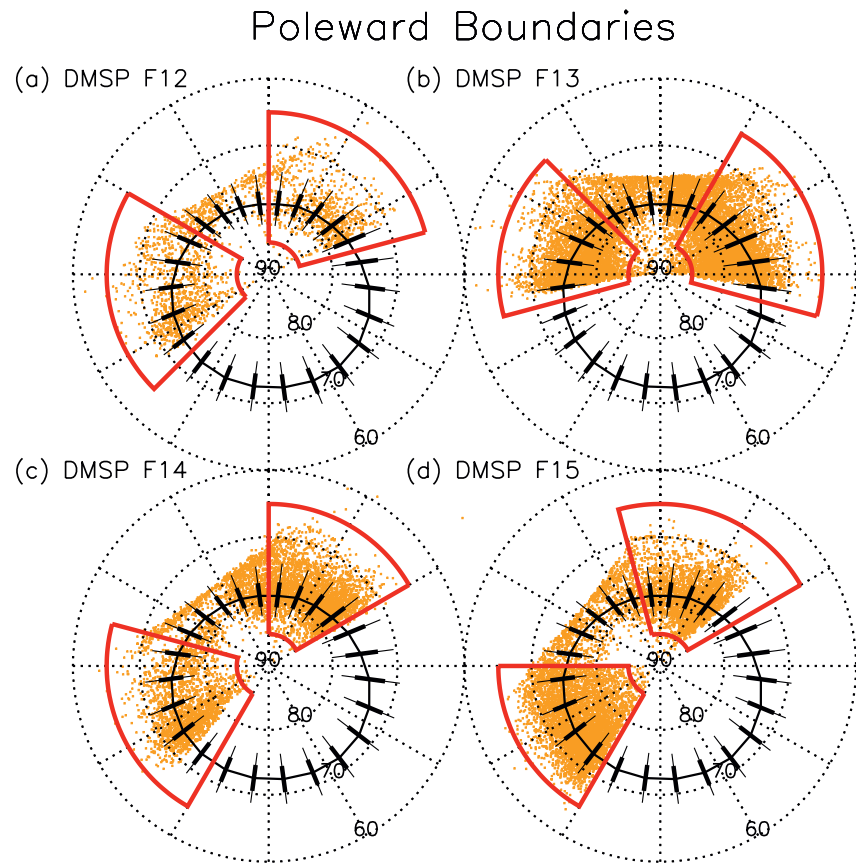
Poleward Boundaries

Figure 4. The locations of DMSP OCB proxies (orange dots) through the measurement epoch, in AACGM and MLT co-ordinates. The black line and error bars show the median and quartile variation of the SI13 PALB data set for reference. The red lines define areas within which the DMSP OCB estimates are most reliable.

over a greater time interval in the data making it more difficult to unambiguously determine the boundary location, and increasing the uncertainty in its estimate. In addition, if the boundary latitude is fluctuating during the spacecraft pass, then multiple, complex crossings may be observed in these regions. This is another reason why we have not used these DMSP OCB estimates.

Following the methodology of Longden et al. (2010), for each DMSP OCB latitude estimate at time t (λ_{OCB}(MLT, t)) we identify the latitude of the closest PALB ($\lambda_P(i, MLT, t)$) for each FUV imager i that is within ±5 min UT and within ±0.5 hr MLT. The latitudinal difference between these two boundaries ($\Delta\lambda_P(i, MLT, t)$) is determined from

$$\Delta\lambda_P(i, MLT, t) = \lambda_P(i, MLT, t) - \lambda_{OCB}(MLT, t) \tag{1}$$

These latitudinal differences are not constant at a particular MLT throughout the data set, partly due to the presence of instrumental and algorithmic noise.

Subsequently, for each MLT sector the distributions of the estimates of $\Delta\lambda_P(i, MLT, t)$ for the complete data set are compiled. From these difference distributions, both Boakes et al. (2008) and Longden et al. (2010) took the modes of the distributions to provide the best estimates for the statistical offsets in each MLT sector. These difference distributions are now typically Gaussian (due to the removal of unreliable DMSP OCB boundary estimates), which suggests that the uncertainties are random, and that the average value provides the best estimate of the typical offset. As the distributions are broadly symmetrical, we choose here to use the median value of the offset in each MLT sector, as it is more accurately determined than the mode. Median values are only determined for MLT sectors where the difference distribution is comprised of at least 100 values. Hence, for each imager, in each MLT sector, the statistical offset is defined as
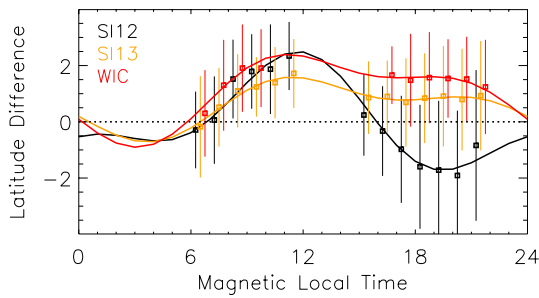
Figure 5. The variation of the median offsets between the IMAGE FUV PALBs and the DMSP OCBs in each 1-hr MLT sector, for the SI12 (black), SI13 (orange), and WIC (red) imagers. The error bars present the quartile range of the offsets (separated slightly in MLT for clarity). The solid lines present the harmonic function fits to the median values for each imager.

$$\Delta\lambda_P(i, MLT) = \text{Median}\left(\Delta\lambda_P(i, MLT, t)\right) \quad (2)$$

In Figure 5 the values of $\Delta\lambda_p(i, \text{MLT})$ are presented. The black, orange, and red squares represent the values for the SI12, SI13, and WIC imagers, respectively. The error bars represent the quartile range of the distributions at each MLT. Owing to the orbits of the DMSP spacecraft in the northern hemisphere (see Figure 4), the median offsets are restricted to two MLT sectors covering the late morning (06:00–12:00 MLT) and dusk (15:00–22:00 MLT) sectors. In the morning sector the median offsets for the three imagers are within 1° of each other, and in the late morning the OCB lies on average ~2° equatorward of the PALBs. This is because aurora associated with the cusp region typically exist poleward of the OCB around noon. In the late afternoon the median offset for the SI12 proton aurora boundary diverges significantly from those for SI13 and WIC by ~2–3°. Consequently, the SI12 PALB lies on average equatorward of the OCB in this region, whereas the other PALBs lie on average poleward of the OCB.

In order to provide the best estimate of the statistical offsets for each imager at all MLTs, we model the median offsets as a function of MLT using a second-order harmonic function (as in Carbary et al., 2003; Boakes et al., 2008; Longden et al., 2010) given by

$$L(\phi) = C_0 + C_1 \cos\phi + D_1 \sin\phi + C_2 \cos 2\phi + D_2 \sin 2\phi \quad (3)$$

where ϕ represents MLT as an angle (MLT $\times$ 15°), starting with 0° at midnight, and increasing toward dawn with increasing MLT, and C_0, C_1, C_2, D_1, and D_2 are the coefficients of the fit. The best fits, and hence the coefficients for each imager, are determined using the Levenberg-Marquardt least squares fitting routine. In Figure 5 the black, orange, and red lines represent the resulting fits for the SI12, SI13, and WIC imagers, respectively. The coefficients of the fits for each imager are presented in Table 1. These coefficients allow the determination of the poleward boundary offset $L_P(i, \phi)$ at all MLTs for each imager.

As discussed previously, the earlier studies of Boakes et al. (2008) and Longden et al. (2010) produced separate estimates of the OCB for each imager, based on a combination of similarly estimated offsets from the DMSP OCBs and statistical intercomparisons between the imager data sets. Here, we combine the estimated PALB measurements from all the available imagers from any one time to provide a single OCB estimate for that time. We use the fitted offset curves for each imager, $L_P(i, \phi)$, in combination with the observed PALBs to determine our OCB estimate using

$$\lambda_{OCB}(\phi, t) = \sum_{i=1}^{n} \frac{\lambda_P(i, \phi, t) - L_P(i, \phi)}{n} \quad (4)$$

where n represents the number of available imagers. For times and MLTs where data from not all PALBs are available, we just use those that are.

A summary of the new OCB data base is presented in Figure 6. As with the PALB statistics, the solid black line shows the variation of the median OCB latitude with MLT. The thick black error bars at each MLT show the latitude range from the lower to the upper quartile of the OCB latitudes, whereas the thinner bars show the latitude range from the 10%–90% percentiles. Again, the orange histogram represents the number of boundaries derived in each MLT sector across the whole measurement epoch. As with the PALBs from which these boundaries are derived, there are a larger number of boundaries in the nightside ionosphere (~10^5), where the auroral emissions are strongest and dayglow weakest.

This new data set is labeled OCB_v2 in the directory "raw_boundaries" at https://doi.org/10.5285/fa592594-93e0-4ee1-8268-b031ce21c3ca (Chisham, 2022). Those who wish to use estimates of the OCB determined

Table 1
The Harmonic Function Fit Coefficients for the OCB Offsets From the Imager PALBs (Equation 3)

Imager	C_0	C_1	D_1	C_2	D_2
SI12	0.0405	−1.5078	0.5095	0.9371	0.0708
SI13	0.5797	−0.6837	−0.5020	0.2971	−0.4173
WIC	1.0298	−1.1249	−0.7380	0.1838	−0.6171

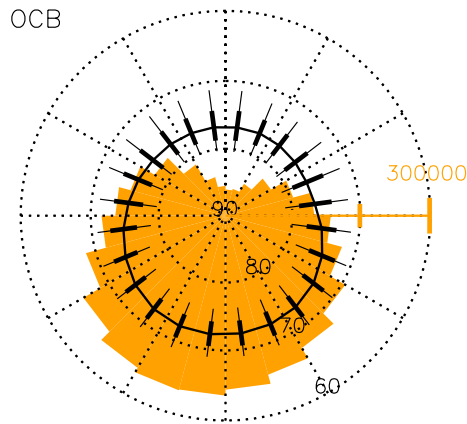*Note.* These define L_P for each imager.

Figure 6. Statistics of OCB locations derived from the IMAGE FUV PALBs in AACGM co-ordinates. The solid black line describes the MLT variation of the median OCB latitude. The thick black error bars present the quartile latitude variation at each MLT. The thin black error bars at each MLT present the extent of the distribution from the 10%–90% percentile. The orange histograms present the number of OCB estimations in each MLT sector.

from a single imager only rather than from the combined data sets can do so using the relevant PALB and the offsets described by Equation 3 and Table 1.

4.4. EALB

A summary of the new EALB data base is presented in Figure 7. As with the PALB statistics, the solid black line shows the variation of the median EALB latitude with MLT for each imager: (a) SI12, (b) SI13, and (c) WIC. The thick black error bars at each MLT show the latitude range from the lower to the upper quartile of the measured EALB latitudes, whereas the thinner bars show the latitude range from the 10%–90% percentiles. The variations for the three imagers show greater differences than with the PALB median latitude variation, with the shape of the median SI12 (proton aurora) EALB being distinctly different to that of the median SI13 and WIC (electron aurora) EALBs (which are similar). The median SI12 boundary extends further equatorward in the early afternoon sector, whereas the median SI13 and WIC boundaries extend further equatorward in the late morning sector. This is likely owing to the different equatorward extents of the electron and proton precipitation in the morning and afternoon sectors.

The orange histograms in each panel represent the number of boundaries measured in each MLT sector across the whole measurement epoch. As with the PALBs a larger number of boundaries are measured in the nightside ionosphere where the auroral emissions are strongest. Again, the number of boundaries decreases significantly toward noon, where the effect of dayglow on the ability to identify EALBs is greater than on the PALBs. These variations were not presented for the original data set in Longden et al. (2010), although they were similar to those for the PALBs. Again, the new criteria employed here better identify potentially erroneous boundaries within the original Longden et al. (2010) data set.

The data bases are located in the files EALB_SI12_v2, EALB_SI13_v2, and EALB_WIC_v2 in the directory "raw_boundaries" at https://doi.org/10.5285/fa592594-93e0-4ee1-8268-b031ce21c3ca (Chisham, 2022).

4.5. EPB

This is the first time that a proxy for the EPB has been estimated indirectly from auroral imager data. This is achieved using statistical latitudinal offsets that have been determined through a comparison of the measured EALBs with the DMSP "b1e"/"b2i" and "deq" EPBs discussed above. As with the derivation of the OCB proxy presented earlier, we are selective about which DMSP EPB data are used in the comparison with the EALBs. Figure 8 displays as orange dots the locations of all the EPB estimates identified by the four different DMSP spacecraft used in this study (DMSP F12, F13, F14, and F15). As with the DMSP OCBs, the boundaries again
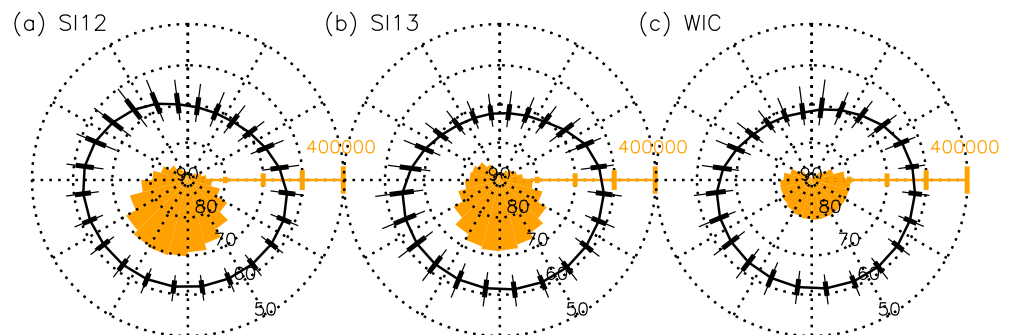

Figure 7. Statistics of EALB locations from the IMAGE FUV imagers (a) SI12, (b) SI13, and (c) WIC, in AACGM and MLT co-ordinates. The solid black line describes the MLT variation of the median EALB latitude. The thick black error bars present the quartile latitude variation at each MLT. The thin black error bars at each MLT present the extent of the distribution from the 10%–90% percentile. The orange histograms present the number of EALB observations in each MLT sector.
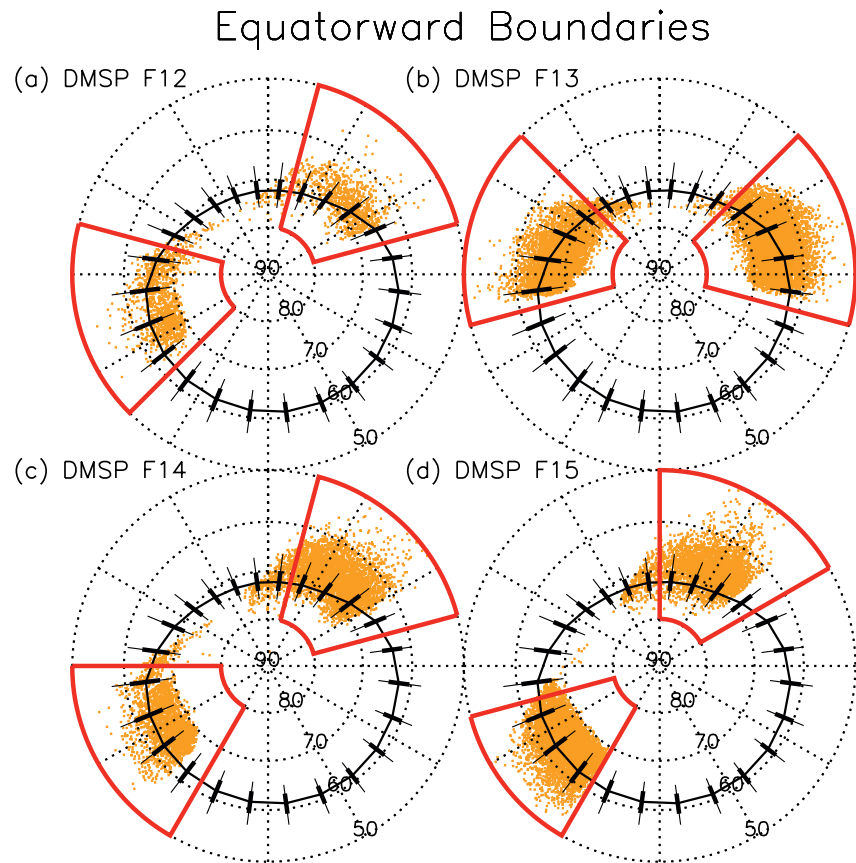
Equatorward Boundaries

Figure 8. The locations of DMSP EPB proxies (orange dots) through the measurement epoch, in AACGM and MLT co-ordinates. The black line and error bars show the median and quartile variation of the SI13 EALB data set for reference. The red lines define areas within which the DMSP EPB estimates are most reliable.

appear in fixed bands across the polar region dictated by the spacecraft orbits and the co-ordinate transform from geographic to AACGM and MLT. The black solid line and error bars show the variation of the median and quartile SI13 EALBs with MLT, as presented previously in Figure 7b. The red sectors highlight where the DMSP EPB estimates are most reliable, following the rationale described for the DMSP OCBs.

We follow the same methodology as with the OCB boundary determination in order to provide estimates of the statistical EPB offsets from the EALBs measured by each imager at all MLTs, modeling the median offsets as a function of MLT using the second-order harmonic function given in Equation 3. Figure 9 presents the median offsets with the associated quartile ranges, and the estimated fits for the model offsets $L_E(i, \phi)$; the black, orange, and red symbols and lines represent the variations for the SI12, SI13, and WIC imagers, respectively. The coefficients of the fits for each of the different imagers are presented in Table 2.

Following the same methodology as with the determination of the OCB proxy, we combine the estimated EALB measurements from the different imagers from any one time to provide a single EPB estimate for that time, using an equatorward boundary version of Equation 4,
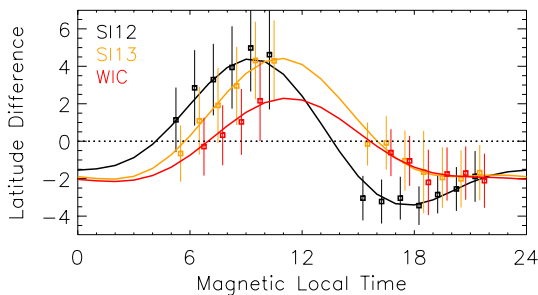
$$\lambda_{EPB}(\phi, t) = \sum_{i=1}^{n} \frac{\lambda_E(i, \phi, t) - L_E(i, \phi)}{n} \tag{5}$$

Again, for times and MLTs where boundaries from not all the imagers are available, we just use those that are.

Figure 9. The variation of the median offsets between the IMAGE FUV EALBs and the DMSP EPBs in each 1-hr MLT sector, for the SI12 (black), SI13 (orange), and WIC (red) imagers. The error bars present the quartile range of the offsets (separated slightly in MLT for clarity). The solid lines present the harmonic function fits to the median values for each imager.

Table 2
The Harmonic Function Fit Coefficients for the EPB Offsets From the Imager EALBs (Equation 3)

Imager	C_0	C_1	D_1	C_2	D_2
SI12	−0.1447	−1.9779	2.6799	0.5778	−1.2297
SI13	0.2500	−2.9931	0.8818	0.8511	−0.6300
WIC	−0.4935	−2.1186	0.3188	0.5749	−0.3118

Note. These define L_E for each imager.

A summary of the new EPB data base is presented in Figure 10. As with previous figures, the black solid line shows the variation of the median EPB latitude with MLT. The thick black error bars at each MLT show the latitude range from the lower to the upper quartile of the EPB latitudes, whereas the thinner bars show the latitude range from the 10%–90% percentiles. Again, the orange histogram represents the number of boundaries derived in each MLT sector across the whole measurement epoch. The most striking difference between the EPB and EALB variations is that the poleward excursion of the EALBs around noon has been significantly reduced due to the offset between the two boundaries that is typically observed there (see Figure 9). The resulting median EPB variation is therefore more circular in shape.

This data set is labeled EPB_v2 in the directory "raw_boundaries" at https://doi.org/10.5285/fa592594-93e0-4ee1-8268-b031ce21c3ca (Chisham, 2022). Those who wish to use estimates of the EPB determined from a single imager only rather than from the combined data sets can do so using the relevant EALB and the offsets described by Equation 3 and Table 2.

5. Fitted Circle Boundary Methodology and Data Sets

Here, we present new circle fits for all the boundary data sets described above, including new improved criteria for helping to identify acceptable fits, an assessment of the suitability of circle fits for each data set, and a validation of the OCB circle fits.

5.1. Methodology

As discussed earlier, boundaries modeled as circles can be very useful in the development of high-latitude ionospheric climatologies and empirical models (Chisham, 2017a). Circles represent simple and practical model functions, and an easily scalable representation of the boundary locations at all MLTs. These model circles also provide a method for filling gaps in those MLT sectors where data is missing, particularly on the dayside where dayglow is a major issue; fitting circles to the MLT variations of the observed boundaries at any one time provides a model description of that boundary at all MLTs.

The circle fitting method employed here is the modified least squares method of Umbach and Jones (2003) as used by Chisham (2017a). This method does not require the location of the center of the circle to be specified in advance. The fitted circles are subsequently defined by three parameters; two which define the co-ordinates of the center of the circle relative to the AACGM pole, and one that defines the circle radius. In the data sets, the fitted circles are described by the following three variables: r_{cent} is the co-latitude distance from the AACGM pole to the fitted circle center; ϕ_{cent} is the MLT angle (MLT × 15°) of the line from the AACGM pole to the fitted circle center; and r_{circ} is the radius of the fitted circle in co-latitude from the fitted circle center.

The circle data sets are labeled PALB_si12_circle_v2, PALB_si13_circle_v2, PALB_wic_circle_v2, OCB_circle_v2, EALB_si12_circle_v2, EALB_si13_circle_v2, EALB_wic_circle_v2, and EPB_circle_v2, in the directory "circle_fit_boundaries" at https://doi.org/10.5285/fa592594-93e0-4ee1-8268-b031ce21c3ca (Chisham, 2022).

5.2. Circle Fit Acceptance Criteria

In the original study of Chisham (2017a), criteria were developed to discard poor, unrealistic or erroneous circle fits of the PALBs and OCB. These criteria were derived from visual inspection of the probability distributions of the fitted parameters, and how these distributions varied with the number of 1-hr MLT sectors *n* where PALBs were contributing to the fit (from the
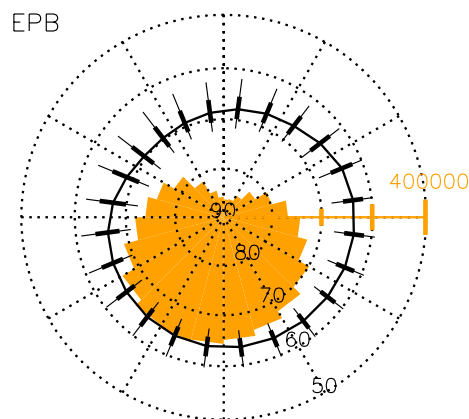

Figure 10. Statistics of EPB locations derived from the IMAGE FUV EALBs in AACGM co-ordinates. The solid black line describes the MLT variation of the median EPB latitude. The thick black error bars present the quartile latitude variation at each MLT. The thin black error bars at each MLT present the extent of the distribution from the 10%–90% percentile. The orange histograms present the number of EPB estimations in each MLT sector.
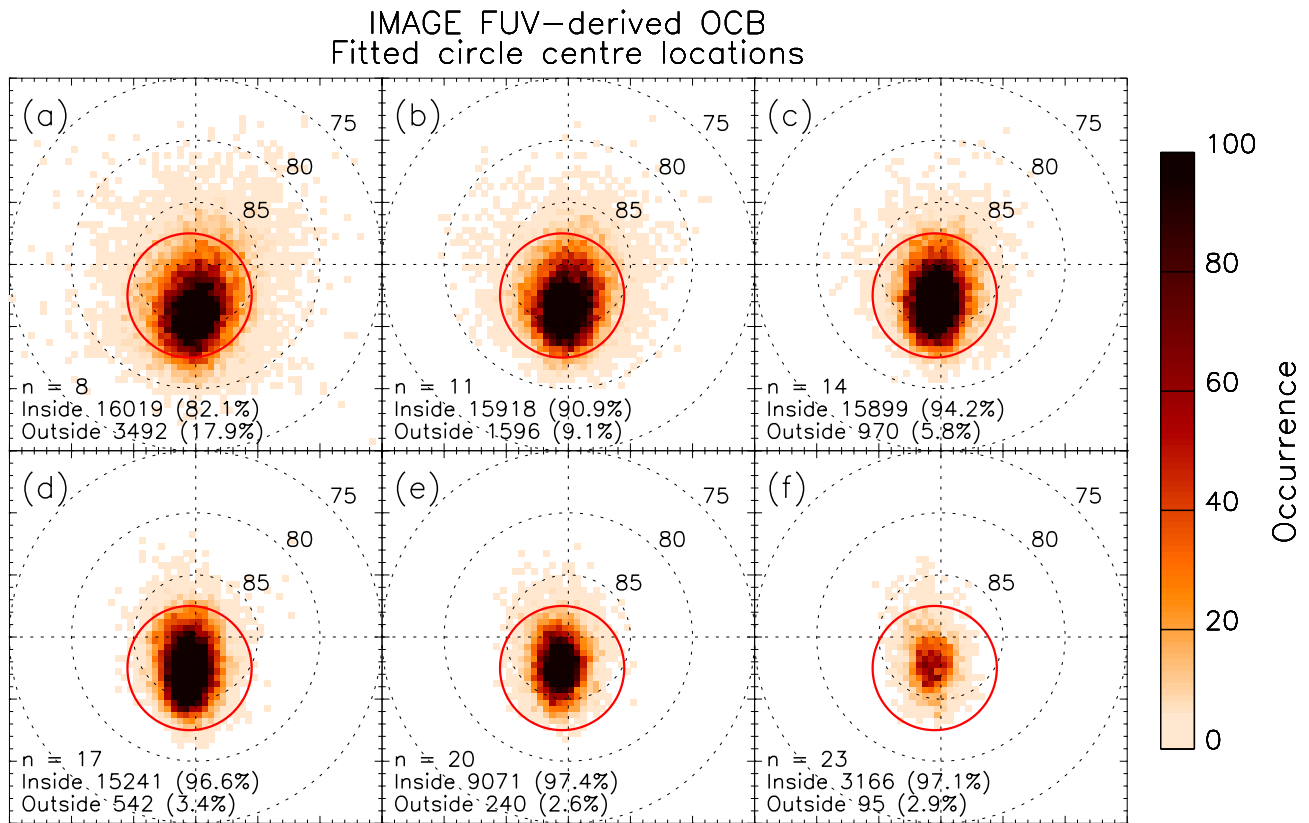
Figure 11. Contour map showing the level of occurrence of OCB fitted circle center locations in AACGM co-ordinates for different numbers of MLT sectors contributing to the fit: (a) 8, (b) 11, (c) 14, (d) 17, (e) 20, and (f) 23. The red circles represent the chosen criteria circles within which the associated fitted circles are thought to be more reliable. The text outlines the number (and percentage) of fitted circle centers that are located inside and outside of the red criteria circle. The co-ordinate system is AACGM with 1200 MLT (noon) to the top of each panel.

minimum of $n = 4$ needed for a minimal circle fit to the maximum $n = 24$, when estimates were available at all MLTs). The criteria for acceptance were set at $n > 7$, $r_{cent} \leq 8°$, and $10° < r_{circ} \leq 22°$. (The last of these criteria is obviously only applicable for the poleward boundaries). However, as the PALB circle centers are predominantly shifted anti-sunward of the AACGM pole, these criteria failed to remove many potentially erroneous fits where the circle centers were shifted significantly sunward of the pole.

In order to more effectively address this issue, here we recommend new criteria, based on the two-dimensional spatial distributions of the fitted circle centers, and how they vary with n. This is in addition to the $n > 7$ criterion. Figure 11 presents contour plots of the occurrence of the locations of the circle centers for the fitted circles derived from the OCB boundary data set for six different values of n (8, 11, 14, 17, 20, and 23), in AACGM co-ordinates. In each panel of the figure there is a preferred region for the location of the circle centers where the occurrence is high (dark orange/black region). The spread of circle centers outside of this region reduces with increasing n, suggesting that there is increasing uncertainty in the circle center estimates away from this core region, especially for lower values of n.

To deal with the increased uncertainty associated with fitted circles with centers away from this core region, we define a circular region centred around this core of observations (shown in red in Figure 11). We propose that fitted circles with centers outside of this red "criteria circle" should be viewed with suspicion. These criteria circles have been chosen for each separate boundary data set by visual inspection of the circle center contour maps (such as those in Figure 11) for all values of n. The criteria circles are defined by the co-ordinates of their center (x_{crit}, y_{crit}) on a Cartesian grid, where the x-axis is positive toward dawn (06:00 MLT) and the y-axis is positive toward noon (12:00 MLT), and the radius of the criteria circle (r_{crit}). The Cartesian values of the fitted circle centers (x_{cent}, y_{cent}) are determined from r_{cent} and ϕ_{cent} using:

Table 3
Recommended Values of the Parameters Describing the Criteria Circles to Help Assess the Fitted Circle Reliability for Each Data Set. (See Text for Details)

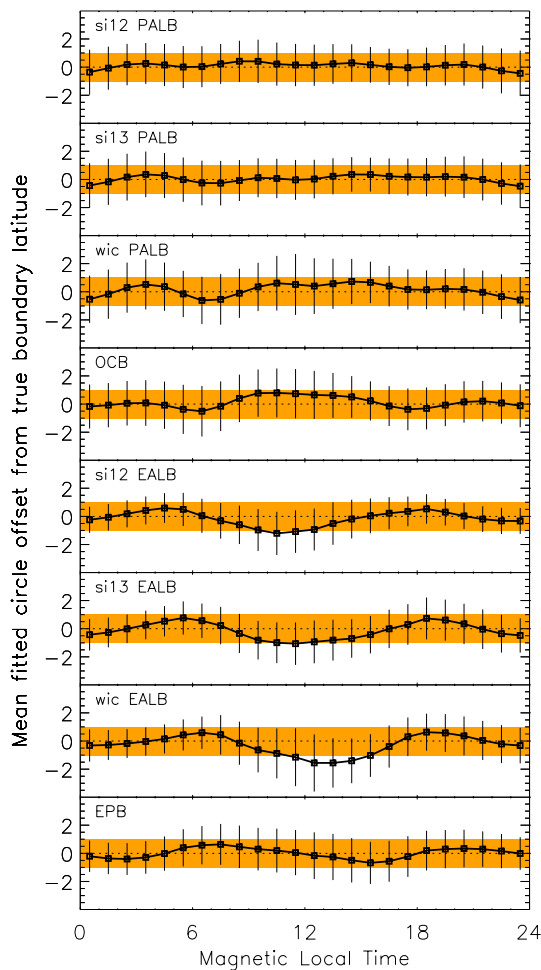| Boundary	x_{crit}	y_{crit}	r_{crit}
SI12 Poleward	−1.5	−3.5	5.0
SI12 Equatorward	−1.0	−3.5	5.0
SI13 Poleward	0.0	−2.5	5.0
SI13 Equatorward	0.0	−5.0	5.0
WIC Poleward	0.0	−3.5	5.0
WIC Equatorward	1.0	−4.0	5.0
OCB	−0.5	−2.5	5.0
EPB	1.0	−2.5	5.0

Figure 12. Comparison of circle fit locations with measured/derived boundary locations. Each panel is labeled with the corresponding boundary data set name. The black symbols and error bars represent the mean and standard deviation of the difference of the fitted circle latitudes from the measured/derived boundary latitudes in each MLT sector, respectively. Hence, the dotted lines at 0° offset represent the relative location of the measured/derived boundary. The orange shading defines the region within which the mean offset is less than 1° latitude.

$$x_{cent} = r_{cent} \sin \phi_{cent} \qquad (6)$$

and

$$y_{cent} = -r_{cent} \cos \phi_{cent}. \qquad (7)$$

To be accepted, we define a merit value r_{merit} for each fitted circle that must satisfy:

$$r_{merit}^2 = (x_{cent} - x_{crit})^2 + (y_{cent} - y_{crit})^2 \leq r_{crit}^2. \qquad (8)$$

The value of r_{merit} for each circle fit also forms part of the data set. Each panel in Figure 11 details the number (and percentage) of fitted circle centers that are located both inside ($r_{merit} < r_{crit}$), and outside ($r_{merit} > r_{crit}$), of the criteria circle. The percentage of values located outside of the criteria circle reduces with increasing n.

The values of x_{crit}, y_{crit}, and r_{crit} estimated for each of the boundary data sets are presented in Table 3. The value of r_{crit} is only a recommendation and can be adjusted to suit the needs of the data user.

5.3. Assessment of Suitability of Circle Fits

The study of Chisham (2017a) contained no assessment of how apt a circle fit was for the observed PALBs. Although the auroral oval is roughly circular when viewed in geomagnetic co-ordinates, there are particular conditions where the poleward boundary is more elliptical than circular. In addition, the equatorward boundary typically diverges significantly from circular on the dayside. Hence, we accept that the circles should generally be viewed as a simple first-order model of the boundaries. However, their simplicity makes them particularly useful for modeling work.

Here, we present a statistical assessment of the suitability of circle model fits for each of the boundary data sets, in order to provide a level of confidence in the model fits. Figure 12 presents, as black square symbols, the MLT variation of the mean difference between the fitted circle locations and the corresponding measured (in the case of the PALBs and EALBs) or derived (in the case of OCBs and EPBs) boundary locations. The error bars show the standard deviation of the boundary differences in each MLT sector. Hence, the dotted line at 0° represents the location of the measured/derived boundaries. The orange region defines where the differences are less than 1°, which we assess as being an acceptable range for the mean offsets, within which the circle model fits are typically a good assumption.

Figure 12 shows that circle fits are particularly suitable for modeling the PALBs, particularly the SI12 and SI13 PALBs, for which the mean offsets are very close to 0° at all MLTs, and for which the standard deviations are approximately 1°. The match for the WIC PALB and the OCB are not as good, particularly around noon. However, all the mean offsets are still less than 1°, with most being less than 0.5°. The circle model fits for the EALBs are not as good, with the fitted circle locations typically lying ~1° equatorward of the measured boundary locations around noon. This is as expected from the typical shape of the equatorward boundary observed on the dayside. This suggests that future studies should consider whether there is a more suitable function for modeling the shape of the EALBs. However, as a result of the large offset between the EALBs and the EPB reported in Figure 9,
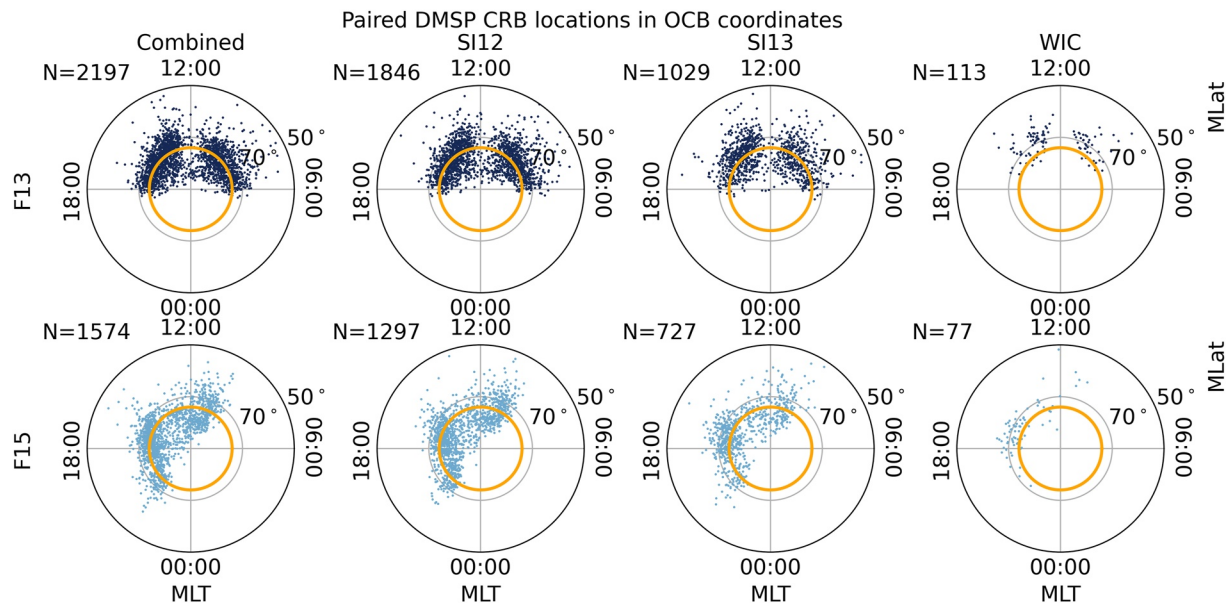
Figure 13. DMSP CRB locations relative to the IMAGE OCB and PALB circle fits (set at 74°, marked by an orange circle) for satellite F13 (top row, navy points) and F15 (bottom row, light blue points). The first column shows the paired CRB and combined OCB data set, while the subsequent columns show the paired boundaries for the SI12, SI13, and WIC PALBs.

the EPB variation is well modeled by a circle, with almost all the mean offsets being less than 0.5°. Overall, we suggest that for most modeling or analysis purposes, that the model circle fits provide a good representation of the boundaries.

5.4. Validation of Poleward Boundaries

The appropriateness of the new PALB and OCB circle fits is further assessed by comparing them to the CRB identified by the plasma convection flow taken from DMSP (Y.-J. Chen et al., 2015; Y.-J. Chen & Heelis, 2018), as was done for the previous IMAGE data base by Burrell, Chisham, Milan, et al. (2020). This validation is limited to MLTs within 05:00–07:00 MLT and 17:00–19:00 MLT to avoid the influence that the IMF has on the plasma convection pattern and the flow reversal boundary locations. The most significant influence is in the region close to the local noon and midnight sectors where magnetic reconnection occurs (see Burrell, Chisham, Milan, et al. (2020) for details). The validation paired the combined (OCB) and individual instrument (PALB) circle fit latitudes with r_{merit} below 5.0° with CRB values identified within 60 s of UT of the OCB/PALB observations. Figure 13 presents the locations of all the DMSP CRBs relative to the circle fit OCBs/PALBs (positioned in the figure at a nominal location of 74°), while the differences between the two boundaries within 1 hr of dawn and dusk are shown in Figure 14.

With the exception of the WIC PALB histogram (which does not have enough points to draw statistically significant conclusions from) the combined OCB, SI12 PALB, and SI13 PALB histograms all have means and medians that are roughly equal with similar standard deviations. The combined OCB and SI12 PALB histograms are centered very close to zero, with no notable skew or kurtosis. The SI13 PALB histogram, however, has a small negative offset and a negative skew. This is to be expected given the observed median offsets between the SI13 PALB and the OCB as shown in Figure 5.

Comparing these results to those presented in Burrell, Chisham, Milan, et al. (2020) shows that the new circle fits and their selection criteria result in less pairings for SI12 and SI13 (the old boundaries had 744 pairings for SI12 and 434 pairings for SI13). However, the statistics are similar; SI12 still has a positive central bias while SI13 has a negative central bias. The mean and median values for the new SI12 and SI13 boundary differences are higher than for the old boundary differences, though not by a significant amount (previously means were 0.32° for SI12 and −0.13° for SI13). However, the Burrell, Chisham, Milan, et al. (2020) analysis used PALBs adjusted by the derived offset to the OCB in the comparison, whereas here we use the unadjusted PALBs.
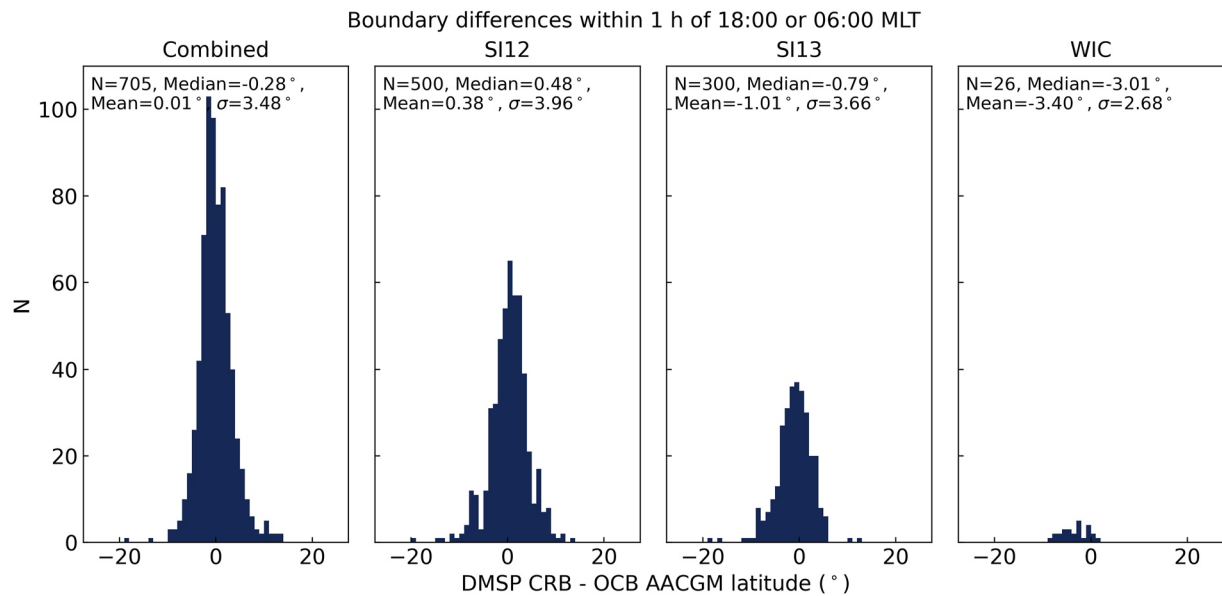
Figure 14. Histogram of differences between the DMSP CRB locations from both F13 and F15 and the OCB/PALB for times within 05:00–07:00 MLT and 17:00–19:00 MLT. The first column shows the histogram and key statistics for the combined OCB data set, while the subsequent columns show the histograms and key statistics for the SI12, SI13, and WIC PALBs.

The new combined OCB data set shows the best agreement with the DMSP CRBs when compared to the new individual PALBs and the old data set. It has the largest number of boundary pairings, with the central statistics closest to zero, and the smallest significant standard deviation. This improved agreement provides confidence in the combined OCB data set, which now matches the performance of the AMPERE OCB proxy (where the mean difference was $-0.01°$ in the northern hemisphere and $-0.02°$ in the southern hemisphere).

6. Summary and Conclusions

This study presents improved poleward and equatorward auroral luminosity boundary estimates from the IMAGE FUV instruments, as well as new estimates of the OCB and EPB. The newly derived OCBs and EPBs provided here have benefited from improved data selection when determining the IMAGE PALBs and EALBs, respectively. New data bases of model circle fits to the MLT variation of the measured/derived boundaries have benefited from a new figure of merit (r_{merit}), that helps to assess the reliability of the fit. The new circle fit OCBs and PALBs have been validated against an independent polar cap boundary proxy. The results of this validation show that the combined OCB data set performs better than previous IMAGE boundary data sets, and matches the performance of other existing OCB proxies.

Modeling and statistical studies of ionospheric, thermospheric, and magnetospheric processes should avoid mixing data from inside the polar cap, within the auroral oval, and equatorward of the auroral oval when determining averages, typical values, or typical conditions. The boundaries provided here and the software that comprises OCBpy provide a set of tools that could be used to improve studies in these regions as well as developing tools for space weather modeling. Future missions with similar imaging capabilities (such as SMILE), could contribute in this area by applying the methods presented here to data from their own instruments.

Data Availability Statement

edu/image/. We thank Tom Sotirelis (Johns Hopkins University, Applied Physics Laboratory) for providing the DMSP boundary data base.

References

Aikio, A. T., Pitkanen, T., Kozlovsky, A., & Amm, O. (2006). Method to locate the polar cap boundary in the nightside ionosphere and application to a substorm event. *Annals of Geophysics*, *24*(7), 1905–1917. https://doi.org/10.5194/angeo-24-1905-2006

Anderson, B. J., Korth, H., Waters, C. L., Green, D. L., Merkin, V. G., Barnes, R. J., & Dyrud, L. P. (2014). Development of large-scale Birkeland currents determined from active magnetosphere and planetary electrodynamics response experiment. *Geophysical Research Letters*, *41*(9), 3017–3025. https://doi.org/10.1002/2014gl059941

Baker, J. B., Clauer, C. R., Ridley, A. J., Papitashvili, V. O., Brittnacher, M. J., & Newell, P. T. (2000). The nightside poleward boundary of the auroral oval as seen by DMSP and the ultraviolet imager. *Journal of Geophysical Research*, *105*(A9), 21267–21280. https://doi.org/10.1029/1999ja000363

Blanchard, G. T., Ellington, C. L., Lyons, L. R., & Rich, F. J. (2001). Incoherent scatter radar identification of the dayside magnetic separatrix and measurement of magnetic reconnection. *Journal of Geophysical Research*, *106*(A5), 8185–8195. https://doi.org/10.1029/2000ja000262

Blanchard, G. T., Lyons, L. R., Samson, J. C., & Rich, F. J. (1995). Locating the polar cap boundary from observations of 6300 Å auroral emission. *Journal of Geophysical Research*, *100*(A5), 7855–7862. https://doi.org/10.1029/94ja02631

Boakes, P. D., Milan, S. E., Abel, G. A., Freeman, M. P., Chisham, G., & Hubert, B. (2009). A statistical study of the open magnetic flux content of the magnetosphere at the time of substorm onset. *Geophysical Research Letters*, *36*(4), L04105. https://doi.org/10.1029/2008GL037059

Boakes, P. D., Milan, S. E., Abel, G. A., Freeman, M. P., Chisham, G., & Hubert, B. (2011). A superposed epoch investigation of the relation between magnetospheric solar wind driving and substorm dynamics with geosynchronous particle injection signatures. *Journal of Geophysical Research*, *116*(A1), A01214. https://doi.org/10.1029/2010JA016007

Boakes, P. D., Milan, S. E., Abel, G. A., Freeman, M. P., Chisham, G., Hubert, B., & Sotirelis, T. (2008). On the use of IMAGE FUV for estimating the latitude of the open/closed magnetic field line boundary in the ionosphere. *Annales Geophysicae*, *26*(9), 2759–2769. https://doi.org/10.5194/angeo-26-2759-2008

Burch, J. L. (2000). IMAGE mission overview. *Space Science Reviews*, *91*(1/2), 1–14. https://doi.org/10.1023/a:1005245323115

Burrell, A. G., Chisham, G., Milan, S. E., Kilcommons, L., Chen, Y.-J., Thomas, E. G., & Anderson, B. (2020a). AMPERE polar cap boundaries. *Annales Geophysicae*, *38*(2), 481–490. https://doi.org/10.5194/angeo-38-481-2020

Burrell, A. G., Chisham, G., & Reistad, J. (2020). aburrell/ocbpy: V0.2.1 (0.2.1). *Zenodo*. https://doi.org/10.5281/zenodo.4289226

Carbary, J. F., Sotirelis, T., Newell, P. T., & Meng, C.-I. (2003). Auroral boundary correlations between UVI and DMSP. *Journal of Geophysical Research*, *108*(1018). https://doi.org/10.1029/2002JA009378

Chen, X.-C., Han, D.-S., Lorentzen, D. A., Oksavik, K., Moen, J. I., & Baddeley, L. J. (2017). Dynamic properties of throat aurora revealed by simultaneous ground and satellite observations. *Journal of Geophysical Research*, *122*(3), 3469–3486. https://doi.org/10.1002/2016ja023033

Chen, Y.-J., & Heelis, R. A. (2018). Motions of the convection reversal boundary and local plasma in the high-latitude ionosphere. *Journal of Geophysical Research: Space Physics*, *123*(4), 2953–2963. https://doi.org/10.1002/2017ja024934

Chen, Y.-J., Heelis, R. A., & Cumnock, J. A. (2015). Response of the ionospheric convection reversal boundary at high latitudes to changes in the interplanetary magnetic field. *Journal of Geophysical Research: Space Physics*, *120*(6), 5022–5034. https://doi.org/10.1002/2015ja021024

Chisham, G. (2017a). A new methodology for the development of high-latitude ionospheric climatologies and empirical models. *Journal of Geophysical Research*, *122*(1), 932–947. https://doi.org/10.1002/2016ja023235

Chisham, G. (2017b). Auroral boundary derived from image satellite mission data (May 2000 - October 2002), version 1.1. [Dataset]. Polar Data Centre, Natural Environment Research Council. https://doi.org/10.5285/75aa66c1-47b4-4344-ab5d-52ff2913a61e

Chisham, G. (2022). Ionospheric boundaries derived from IMAGE satellite mission data (May 2000-October 2002), version 2.0. [Dataset]. NERC EDS UK Polar Data Centre. https://doi.org/10.5285/fa592594-93e0-4ee1-8268-b031ce21c3ca

Chisham, G., & Freeman, M. P. (2003). A technique for accurately determining the cusp-region polar cap boundary using SuperDARN HF radar measurements. *Annales Geophysicae*, *21*(4), 983–996. https://doi.org/10.5194/angeo-21-983-2003

Chisham, G., Freeman, M. P., Abel, G. A., Lam, M. M., Pinnock, M., Coleman, I. J., et al. (2008). Remote sensing of the spatial and temporal structure of magnetopause and magnetotail reconnection from the ionosphere. *Reviews of Geophysics*, *46*, RG1004. https://doi.org/10.1029/2007RG000223

Chisham, G., Lester, M., Milan, S. E., Freeman, M. P., Bristow, W. A., Grocott, A., et al. (2007). A decade of the super dual auroral radar network (SuperDARN): Scientific achievements, new techniques and future directions. *Surveys in Geophysics*, *28*(1), 33–109. https://doi.org/10.1007/s10712-007-9017-8

Cowley, S. W. H. (2000). Magnetosphere–ionosphere interactions: A tutorial review. In S. Ohtani (Ed.), *Magnetospheric current systems* (Vol. 118, pp. 91–106). American Geophysical Union. https://doi.org/10.1029/GM118p0091

Cowley, S. W. H., & Lockwood, M. (1992). Excitation and decay of solar wind-driven flows in the magnetosphere–ionosphere system. *Annales Geophysicae*, *10*, 103–115.

Coxon, J. C., Milan, S. E., & Anderson, B. J. (2018). A review of Birkeland current research using AMPERE. In *Electric currents in geospace and beyond* (Vol. 235, pp. 259–278). American Geophysical Union. https://doi.org/10.1002/9781119324522.ch16

Dungey, J. W. (1961). Interplanetary magnetic field and the auroral zones. *Physical Review Letters*, *6*(2), 47–48. https://doi.org/10.1103/physrevlett.6.47

Frey, H. U., Mende, S. B., Angelopoulos, V., & Donovan, E. F. (2004). Substorm onset observations by IMAGE-FUV. *Journal of Geophysical Research*, *109*(A10), A10304. https://doi.org/10.1029/2004JA010607

Gibson, W. C., Burch, J. L., Scherrer, J. R., Tapley, M. B., Killough, R. L., Volpe, F. A., et al. (2000). The IMAGE observatory. *Space Science Reviews*, *91*(1/2), 15–50. https://doi.org/10.1023/a:1005203207186

Gjerloev, J. (2012). The SuperMAG data processing technique. *Journal of Geophysical Research*, *117*(A9), A09213. https://doi.org/10.1029/2012ja017683

Greenwald, R. A., Shepherd, S. G., Sotirelis, T. S., Ruohoniemi, J. M., & Barnes, R. J. (2002). Dawn and dusk sector comparisons of small-scale irregularities, convection, and particle precipitation in the high-latitude ionosphere. *Journal of Geophysical Research*, *107*(A9), 1241. https://doi.org/10.1029/2001JA000158

Hardy, D. A., Schmitt, L. K., Gussenhoven, M. S., Marshall, F. J., Yeh, H. C., Shumaker, T. L., et al. (1984). *Precipitating electron and ion detectors (SSJ/4) for the block 5D/flights 6-10 DMSP satellites: Calibration and data presentation*. Rep. AFGL-TR-84-0317. Air Force Geophysics Lab. Hanscam AFB, Mass.

Heelis, R. A., & Hanson, W. B. (1998). Measurements of thermal ion drift velocity and temperature using planar sensors. In R. F. Pfaff, J. Borovsky, & T. D. Young (Eds.), *Measurement techniques in space plasmas: Particles* (Vol. 102, pp. 61–71). American Geophysical Union.

Hoque, S. N. M. A., Alvi, A., Mahmud, M. R., Sakhawat, S., & Bhuiyan, M. I. (2021). On the use of directional derivatives of SuperDARN convection flow for estimating open-closed field line boundary during the intervals of substorm activity on 14 october 2001. *Polar Science*, *28*, 100655. https://doi.org/10.1016/j.polar.2021.100655

Hubert, B., Aikio, A. T., Amm, O., Pitkanen, T., Kauristie, K., Milan, S. E., et al. (2010). Comparison of the open-closed field line boundary location inferred using IMAGE-FUV SI12 images and EISCAT radar observations. *Annales Geophysice*, *28*(4), 883–892. https://doi.org/10.5194/angeo-28-883-2010

Hubert, B., Milan, S. E., Grocott, A., Blockx, C., Cowley, S. W. H., & Gerard, J.-C. (2006). Dayside and nightside reconnection rates inferred from IMAGE-FUV and super dual auroral radar network data. *Journal of Geophysical Research*, *111*(A3), A03217. https://doi.org/10.1029/2005ja011140

Kauristie, K., Weygand, J., Pulkkinen, T. I., Murphree, J. S., & Newell, P. T. (1999). Size of the auroral oval: UV ovals and precipitation boundaries compared. *Journal of Geophysical Research*, *104*(A2), 2321–2331. https://doi.org/10.1029/1998ja900046

Kilcommons, L. M., Redmon, R. J., & Knipp, D. J. (2017). A new DMSP magnetometer and auroral boundary data set and estimates of field-aligned currents in dynamic auroral boundary coordinates. *Journal of Geophysical Research: Space Physics*, *122*(8), 9068–9079. https://doi.org/10.1002/2016ja023342

Kivelson, M. G., Russell, C. T., & Brown, M. E. (1996). Introduction to space physics. *Physics Today*, *49*(4), 57–58. https://doi.org/10.1063/1.2807586

Lockwood, M. (1998). Identifying the open-closed field line boundary. In J. Moen (Ed.), *Polar cap boundary phenomena* (pp. 73–90). Kluwer Academic Publishers.

Longden, N., Chisham, G., & Freeman, M. P. (2014). Magnetic local time variation and scaling of poleward auroral boundary dynamics. *Journal of Geophysical Research*, *119*(12), 10006–10022. https://doi.org/10.1002/2014ja020430

Longden, N., Chisham, G., Freeman, M. P., Abel, G. A., & Sotirelis, T. (2010). Estimating the location of the open-closed magnetic field line boundary from auroral images. *Annales Geophysicae*, *28*(9), 1659–1678. https://doi.org/10.5194/angeo-28-1659-2010

Mende, S., Heetderks, H., Frey, H., Lampton, M., Geller, S., Abiad, R., et al. (2000). Far ultraviolet imaging from the IMAGE spacecraft. 2. Wideband FUV imaging. *Space Science Reviews*, *91*(1/2), 271–285. https://doi.org/10.1023/a:1005227915363

Mende, S., Heetderks, H., Frey, H., Lampton, M., Geller, S., Habraken, S., et al. (2000). Far ultraviolet imaging from the IMAGE spacecraft. 1. System design. *Space Science Reviews*, *91*(1/2), 243–270. https://doi.org/10.1023/a:1005271728567

Mende, S., Heetderks, H., Frey, H., Stock, J., Lampton, M., Geller, S., et al. (2000). Far ultraviolet imaging from the IMAGE spacecraft. 3. Spectral imaging of the Lyman-α and OI 135.6 nm. *Space Science Reviews*, *91*(1/2), 287–318. https://doi.org/10.1023/a:1005292301251

Milan, S. E. (2009). Both solar wind-magnetosphere coupling and ring current intensity control of the size of the auroral oval. *Geophysical Research Letters*, *36*(18), L18101. https://doi.org/10.1029/2009GL039997

Milan, S. E., Clausen, L. B. N., Coxon, J. C., Carter, J. A., Walach, M.-T., Laundal, K., et al. (2017). Overview of solar wind–magnetosphere–ionosphere–atmosphere coupling and the generation of magnetospheric currents. *Space Science Reviews*, *206*(1–4), 547–573. https://doi.org/10.1007/s11214-017-0333-0

Milan, S. E., Gosling, J. S., & Hubert, B. (2012). Relationship between interplanetary parameters and the magnetopause reconnection rate quantified from observations of the expanding polar cap. *Journal of Geophysical Research*, *117*(A3), A03226. https://doi.org/10.1029/2011JA017082

Milan, S. E., Hutchinson, J., Boakes, P. D., & Hubert, B. (2009). Influences on the radius of the auroral oval. *Annales Geophysicae*, *27*(7), 2913–2924. https://doi.org/10.5194/angeo-27-2913-2009

Milan, S. E., Lester, M., Cowley, S. W. H., Oksavik, K., Brittnacher, M., Greenwald, R. A., et al. (2003). Variations in the polar cap area during two substorm cycles. *Annales Geophysicae*, *21*(5), 1121–1140. https://doi.org/10.5194/angeo-21-1121-2003

Mooney, M. K., Forsyth, C., Rae, I. J., Chisham, G., Coxon, J. C., Marsh, M. S., et al. (2020). Examining local time variations in the gains and losses of open magnetic flux during substorms. *Journal of Geophysical Research*, *125*(4), e2019JA027369. https://doi.org/10.1029/2019ja027369

Mooney, M. K., Marsh, M. S., Forsyth, C., Sharpe, C., Hughes, T., Bingham, S., et al. (2021). Evaluating auroral forecasts against satellite observations. *Space Weather*, *19*, e2020SW002688. https://doi.org/10.1029/2020sw002688

Newell, P. T., Burke, W. J., Sanchez, E. R., Meng, C.-I., Greenspan, M. E., & Clauer, C. R. (1991). The low-latitude boundary layer and the boundary plasma sheet at low altitude: Prenoon precipitation regions and convection reversal boundaries. *Journal of Geophysical Research*, *96*(A12), 21013–21023. https://doi.org/10.1029/91ja01818

Newell, P. T., Feldstein, Y. I., Galperin, Y. I., & Meng, C.-I. (1996). Morphology of nightside precipitation. *Journal of Geophysical Research*, *101*(A5), 10737–10748. https://doi.org/10.1029/95ja03516

Newell, P. T., Liou, K., Zhang, Y., Sotirelis, T., Paxton, L. J., & Mitchell, E. J. (2014). Ovation prime-2013: Extension of auroral precipitation model to higher disturbance levels. *Space Weather*, *12*(6), 368–379. https://doi.org/10.1002/2014SW001056

Newell, P. T., Ruohoniemi, J. M., & Meng, C.-I. (2004). Maps of precipitation by source region, binned by IMF, with inertial convection streamlines. *Journal of Geophysical Research*, *109*(A10), A10206. https://doi.org/10.1029/2004JA010499

Redmon, R. J., Peterson, W. K., Andersson, L., Kihn, E. A., Denig, W. F., Hairston, M., & Coley, R. (2010). Vertical thermal O^+ flows at 850 km in dynamic auroral boundary coordinates. *Journal of Geophysical Research*, *115*(A11), A00J08. https://doi.org/10.1029/2010JA015589

Shepherd, S. G. (2014). Altitude-adjusted corrected geomagnetic coordinates: Definition and functional approximations. *Journal of Geophysical Research*, *119*(9), 7501–7521. https://doi.org/10.1002/2014JA020264

Siscoe, G. L., & Huang, T. S. (1985). Polar cap inflation and deflation. *Journal of Geophysical Research*, *90*(A1), 543–547. https://doi.org/10.1029/ja090ia01p00543

Sotirelis, T., & Newell, P. T. (2000). Boundary-oriented electron precipitation model. *Journal of Geophysical Research*, *105*(A8), 18655–18673. https://doi.org/10.1029/1999ja000269

Umbach, D., & Jones, K. N. (2003). A few methods for fitting circles to data. *IEEE Transactions on Instrumentation and Measurement*, *52*(6), 1881–1885. https://doi.org/10.1109/tim.2003.820472

Zhu, Q., Deng, Y., Richmond, A., Maute, A., Chen, Y.-J., Hairston, M., et al. (2020). Impacts of binning methods on high-latitude electrodynamic forcing: Static vs. boundary-oriented binning methods. *Journal of Geophysical Research*, *125*(1), e2019JA027270. https://doi.org/10.1029/2019JA027270